



Triggering the Untriggered: The First Einstein Probe-detected Gamma-Ray Burst 240219A and Its Implications

Yin et al. 2024, ApJL, 975(2), L27

Reporter: Dan Zhu

2024/11/18

1.Introduction

The Einstein Probe (EP), launched on 2024 January 9, is equipped with two scientific instruments, the Wide-field X-ray Telescope (WXT) and the Follow-up X-ray Telescope (FXT).

On 2024 February 19 at 06:21:42 UT (referred to as T_0), the EP/WXT detected and located a bright X-ray flare named EP240219a during its commissioning phase at R.A. = $80^\circ.031$ and decl. = $25^\circ.533$ (J2000) with an uncertainty of $2'.3$ (Figure 1).

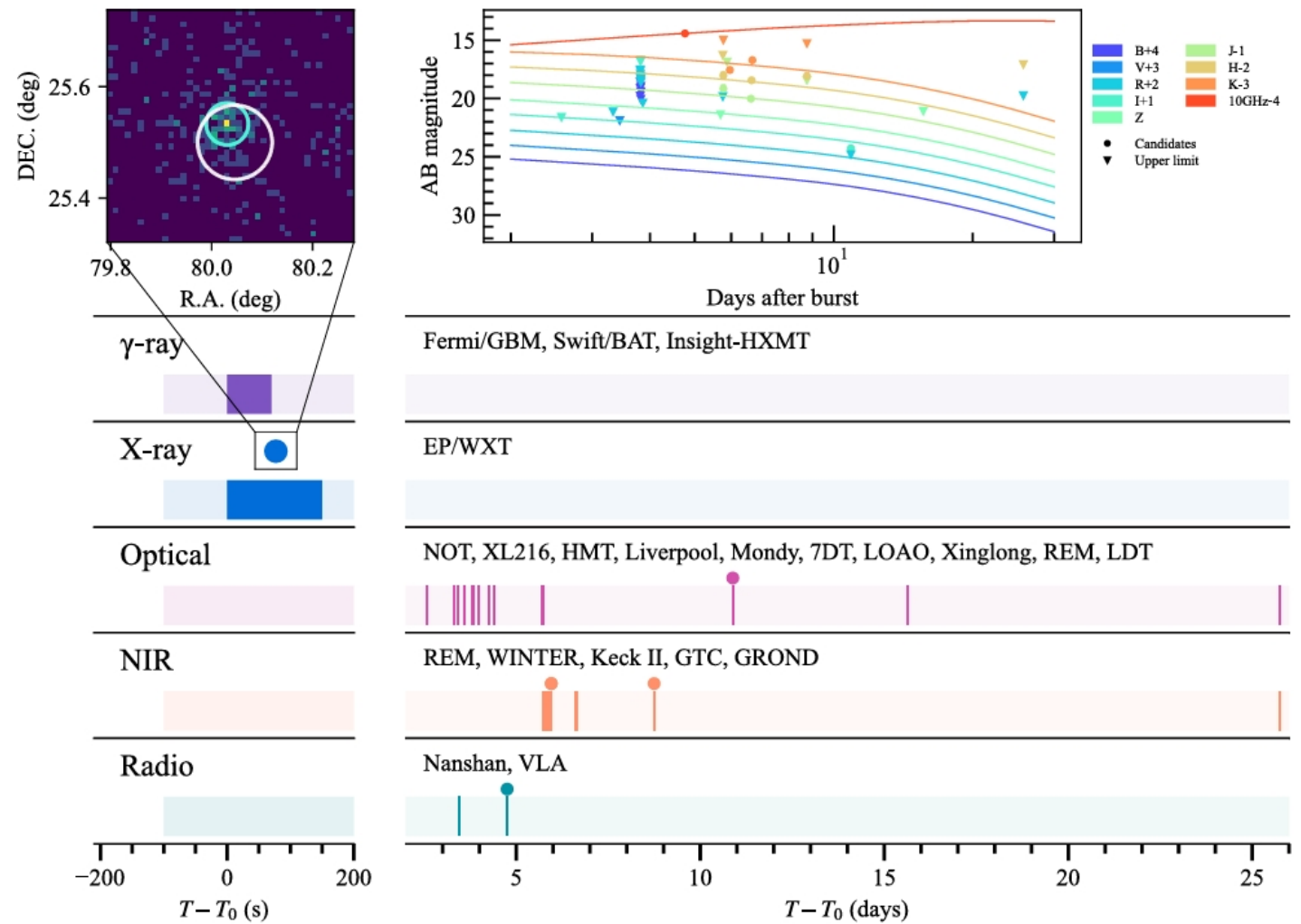


Figure 1. Multiwavelength observations of EP240219a/GRB 240219A. The small dots indicate follow-up observations with candidates, while the lines denote the observing times. The top panels display EP source observation, with the EP/WXT position marked with a light blue circle and the Swift/BAT position marked with a white circle and afterglow detections of Candidate 3 with upper limits.

1. Introduction

The source exhibits an overall profile of a fast-rise and exponential-decay shape and lasts approximately 160s (see Figure 2).

Following the EP alert, a faint, untriggered gamma ray transient that occurred at the same time as T_0 was discovered offline in the archived data of Fermi/GBM, Swift/BAT, Insight-HXMT/HE.

The gamma-ray transient exhibits a total duration of approximately 70s and shared a consistent location with EP240219a, leading to its reclassification as GRB 240219A.

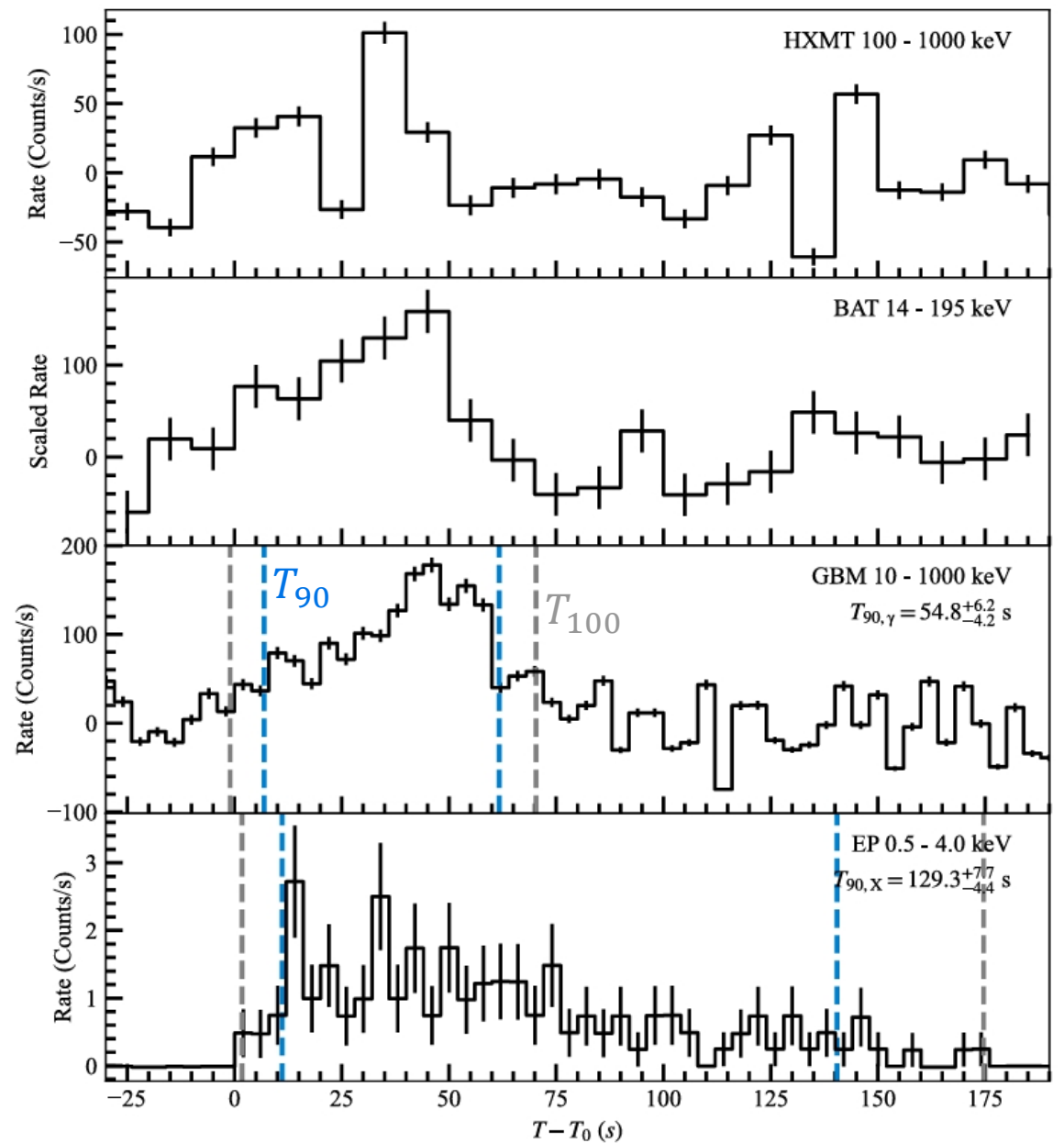


Figure 2. Light curves of GRB 240219A as observed by Insight-HXMT/HE, Swift/BAT, Fermi/GBM, and EP/WXT.

2. DATA REDUCTION AND ANALYSIS

DATA:

EP/WXT data (0.5- 4.0 keV): The source and background light curves and spectra for any specified time interval were obtained from a circular region with a radius of 9.1 arcminutes and an annular region with inner and outer radii of 1.4° and 1.8° , respectively.

Fermi/GBM data (8keV-40MeV): Among the twelve sodium iodide detectors, n9 and na were chosen. Furthermore, for both temporal and spectral analyses, we included the bismuth germanium oxide detector, b1.

2.1 Light Curve

(1) **The duration:** GBM (10–1000 keV): $T_{90,\gamma} = 54.8^{+6.2}_{-4.2}$ s
EP/WXT (10–1000 keV): $T_{90,X} = 129.3^{+7.7}_{-4.4}$ s.

(2) **Spectral lag:** defined as the time delay of high-energy photons with respect to low energy photons. $t_{lag} = -4.0^{+1.1}_{-1.1}$ s.

(3) **The minimum variability timescale (MVT):** is a measurement of the temporal variability of the light curves. For Fermi/GBM data, the MVT was **2.19 s**, whereas for EP/WXT data, it was **29.3 s**.

For GRB 240219A, the MVT and gamma-ray luminosity (assuming redshift $0.5 < z < 4$) exhibit an empirical anti-correlation.

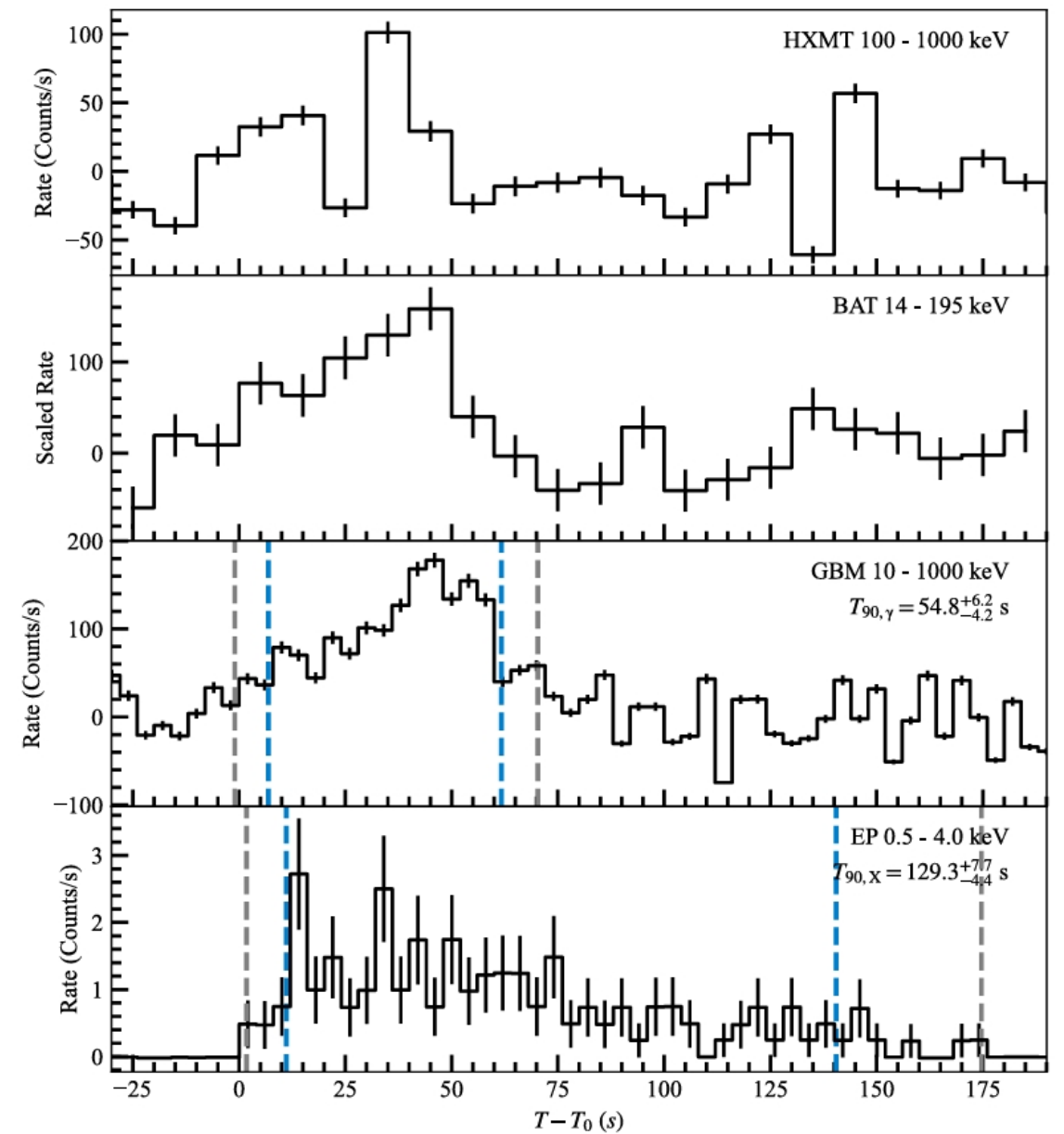


Figure 2. Light curves of GRB 240219A as observed by Insight-HXMT/HE, Swift/BAT, Fermi/GBM, and EP/WXT.

2.2 Spectral Fit

1. The spectral models:

The best-fit model {

- EP/WXT spectra: PL
- Fermi/GBM spectra: cutoff power law (CPL)
- Joint EP/WXT and Fermi/GBM spectral: CPL

2. The N_H value: A fixed N_H value is adopted in all fits. $N_H = 1.03_{-0.21}^{+0.39} \times 10^{22} \text{ cm}^{-2}$.

3. Independent fit.

Time-integrated fit: In the time interval of 0-70 seconds, the time-integrated spectrum of EP/WXT data has an average photon index of $-1.69_{-0.30}^{+0.25}$. The photon index of Fermi/GBM data is $-1.40_{-0.28}^{+0.17}$ and the peak energy is 127_{-32}^{+304} keV.

The photon index of the two detectors is consistent, suggesting a common physical origin of the emissions in the two energy bands.

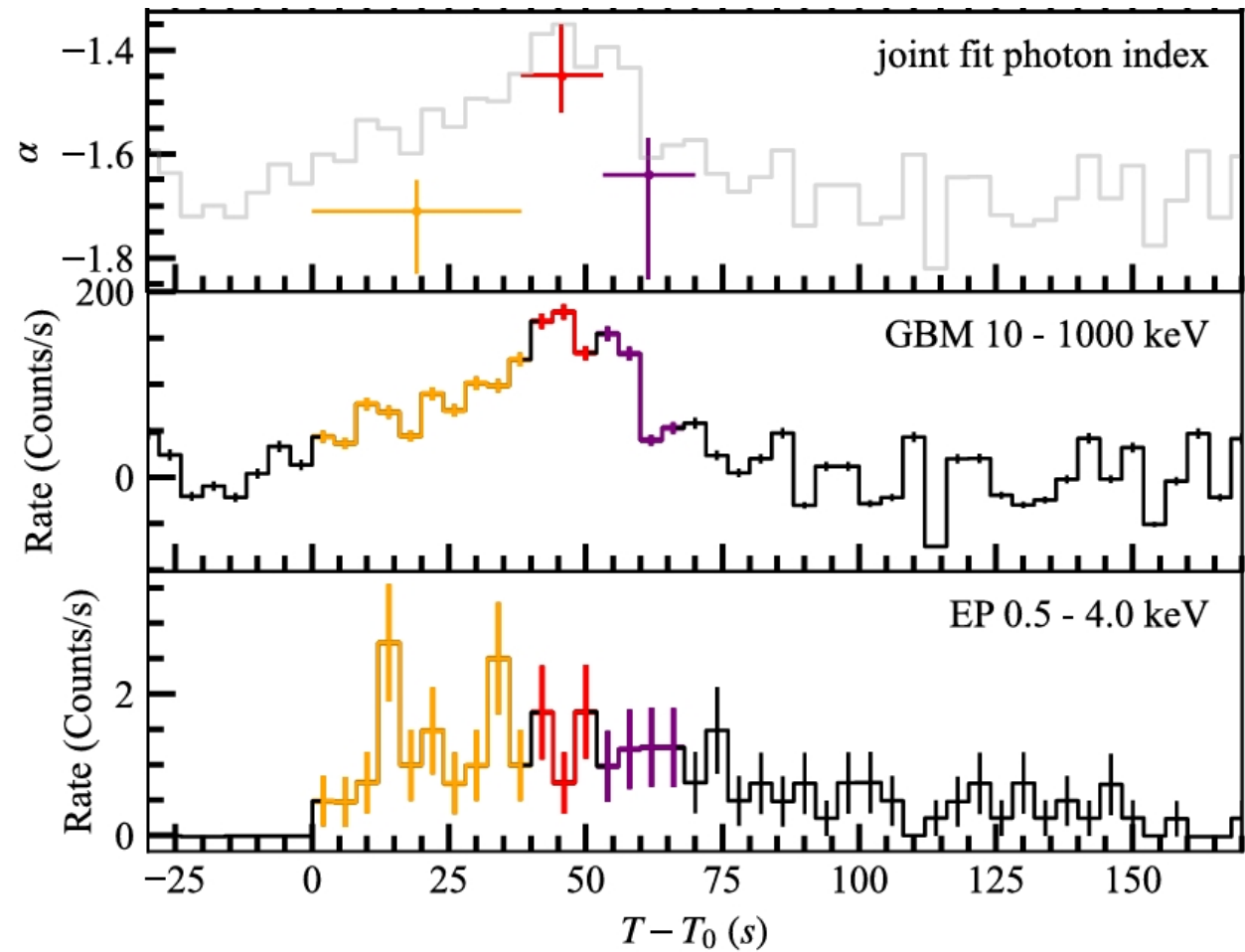
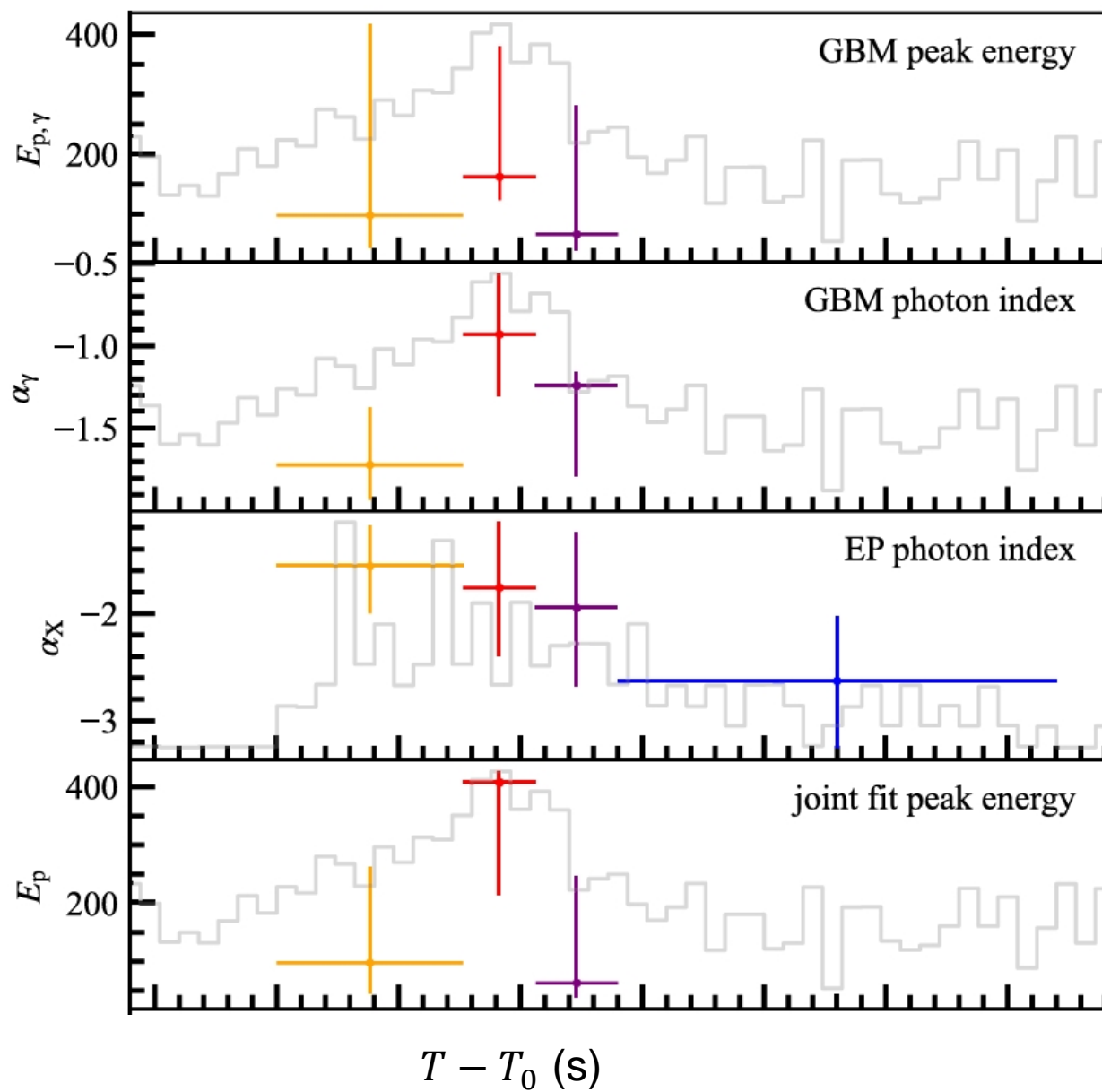


Figure 3. The observed light curves of GRB 240219A and its spectral evolution based on the best-fit parameters.

4. Joint fit.

The left panels present SEDs derived from independent spectral fittings at different time intervals. Solid lines show the best-fit unabsorbed model for each independent fit.

The right panels show SEDs obtained from joint spectral fittings using an absorbed single CPL model at different time intervals.

The uncertainties from joint fit are smaller than those obtained from independent fits. Therefore, we adopt the best fit model parameters of the joint fit for subsequent analyses.

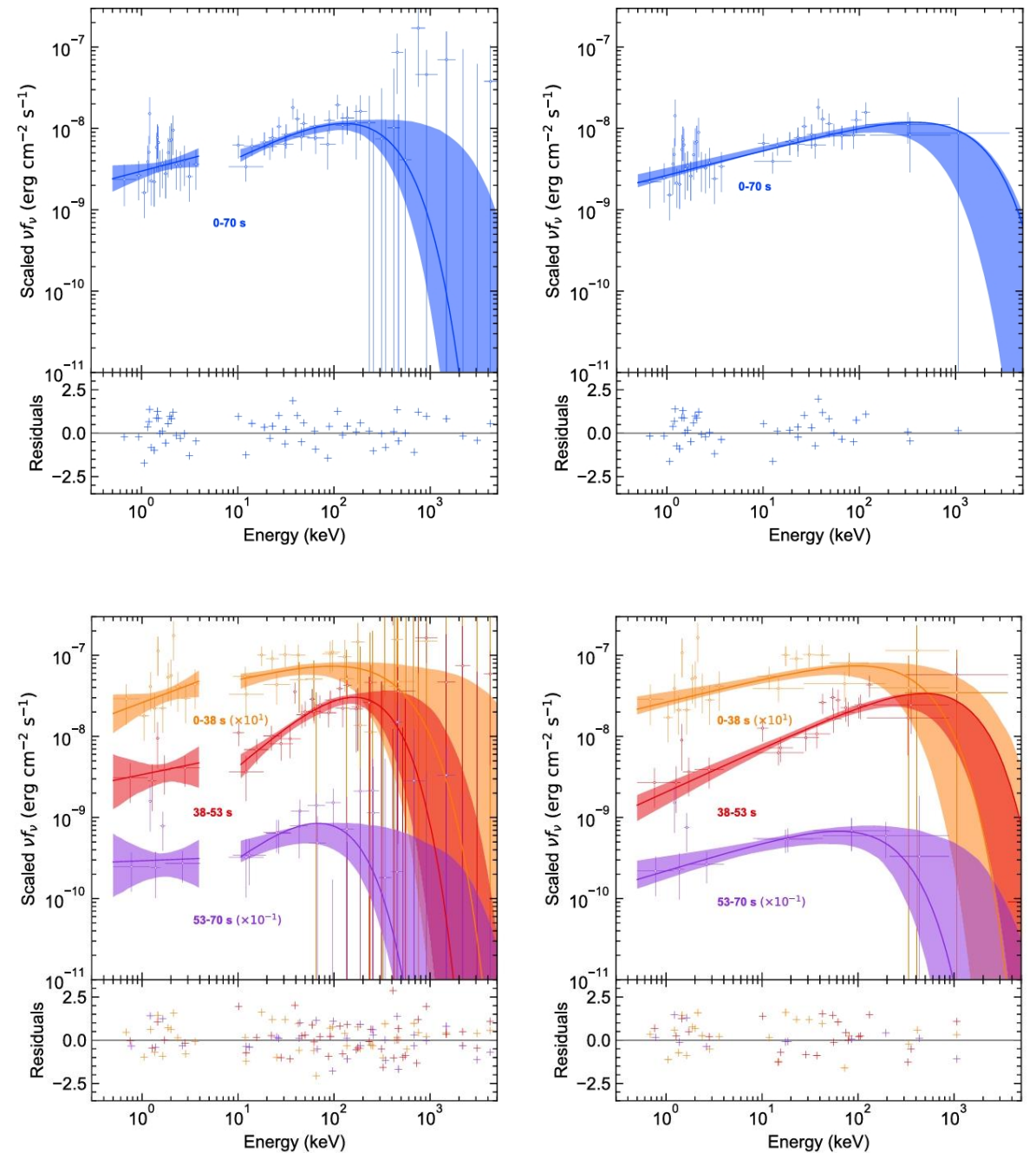


Figure4. SEDs and their evolution.

Table 3
Multiwavelength Follow-up Observations of GRB 240219A

$T - T_0$ (day)	ΔT (s)	(R.A., Decl.)	Telescope	Band	AB Magnitude	Comment	References
0.000	...	(80.031, 25.533)	EP/WXT	x-ray	(1,17)
0.000	Fermi/GBM	Gamma-ray	(2)
0.000	300	(80.046, 25.500)	Swift/BAT	Gamma-ray	(3)
0.000	Insight-HXMT/HE	Gamma-ray	(4)
2.574	3×120	...	Liverpool/IO:O	<i>I</i>	>22.12	...	(5)
3.329	9×200	...	XL216	<i>R</i>	>21.3	...	(6)
3.424	30×90	...	HMT	unfilter	>19.7	...	(17)
3.443	12×200	...	Nanshan	<i>V</i>	>21.7126	...	(7)
3.582	9×200	(80.034, 25.548)	NOT	<i>z</i>	21.8 ± 0.2	candidate 0 (ruled out)	(17)
3.811	900	...	7DT	m400	>18.166	...	(8)
3.824	900	...	7DT	m425	>18.338	...	(8)
3.812	900	...	7DT	m450	>18.330	...	(8)
3.824	900	...	7DT	m475	>18.447	...	(8)
3.811	900	...	7DT	m500	>18.597	...	(8)
3.823	900	...	7DT	m525	>18.678	...	(8)
3.816	900	...	7DT	m550	>18.379	...	(8)
3.828	900	...	7DT	m575	>18.486	...	(8)
3.813	900	...	7DT	m600	>17.712	...	(8)
3.825	900	...	7DT	m625	>18.365	...	(8)
3.812	900	...	7DT	m650	>18.110	...	(8)
3.824	900	...	7DT	m675	>18.425	...	(8)
3.812	900	...	7DT	m700	>17.894	...	(8)
3.824	900	...	7DT	m725	>18.029	...	(8)
3.812	900	...	7DT	m750	>17.154	...	(8)
3.825	900	...	7DT	m775	>17.641	...	(8)
3.815	900	...	7DT	m800	>17.177	...	(8)
3.827	900	...	7DT	m825	>17.014	...	(8)
3.861	60×30	...	LOAO	<i>R</i>	>20.562	...	(9)
4.278	30×120	...	Mondy	<i>R</i>	>18.00	...	(10)
4.278	30×120	...	Mondy	<i>R</i>	>18.63	...	(10)
4.416	30×90	...	HMT	unfilter	>19.5	...	(17)
4.765	2070	(80.046, 25.560)	VLA	<i>X</i>	$169 \mu Jy$	candidate 1 (unlikely)	(11)
4.765	2070	(80.050, 25.535)	VLA	<i>X</i>	$82 \mu Jy$	candidate 2 (unlikely)	(11)
4.765	2070	(80.020, 25.530)	VLA	<i>X</i>	$157 \mu Jy$	candidate 3 (undetermined)	(11)
4.765	2070	(80.025, 25.522)	VLA	<i>X</i>	$38 \mu Jy$	candidate 4 (undetermined)	(11)
4.765	2070	(79.999, 25.546)	VLA	<i>X</i>	$49 \mu Jy$	candidate 5 (undetermined)	(11)
4.765	2070	(80.020, 25.558)	VLA	<i>X</i>	$30 \mu Jy$	candidate 6 (ruled out)	(11)
4.765	2070	(79.969, 25.530)	VLA	<i>X</i>	$300 \mu Jy$	candidate 7 (ruled out)	(11)
5.685	12×200	...	NOT	<i>z</i>	>22.5	...	(17)
5.754	1200	...	REM	<i>r</i>	>19.9	...	(12)
5.754	1200	...	REM	<i>H</i>	>18.69	...	(12)
5.768	1200	...	GROND	<i>J</i>	20.80 ± 0.37	candidate 3	(17)
5.768	1200	...	GROND	<i>H</i>	20.44 ± 0.34	candidate 3	(17)
5.768	1200	...	GROND	<i>K_s</i>	>18.24	candidate 3	(17)
5.877	WINTER	<i>J</i>	>18.5	unknown exposure time	(13)
5.959	4×300	(80.020, 25.530)	Keck II/NIRES	<i>K'</i>	20.84	candidate 3	(14)
6.619	91×10	(80.020, 25.530)	GTC/EMIR	<i>J</i>	21.66 ± 0.10	candidate 3	(17)
6.619	91×10	(80.025, 25.522)	GTC/EMIR	<i>J</i>	>25.86	candidate 4	(17)
6.619	91×10	(79.999, 25.546)	GTC/EMIR	<i>J</i>	22.33 ± 0.11	candidate 5	(17)
6.639	188×6	(80.020, 25.530)	GTC/EMIR	<i>H</i>	20.86 ± 0.10	candidate 3	(17)
6.639	188×6	(80.025, 25.522)	GTC/EMIR	<i>H</i>	>25.92	candidate 4	(17)
6.639	188×6	(79.999, 25.546)	GTC/EMIR	<i>H</i>	21.58 ± 0.09	candidate 5	(17)
6.665	420×3	(80.020, 25.530)	GTC/EMIR	<i>K_s</i>	19.99 ± 0.13	candidate 3	(17)
6.665	420×3	(80.025, 25.522)	GTC/EMIR	<i>K_s</i>	>25.92	candidate 4	(17)
6.665	420×3	(79.999, 25.546)	GTC/EMIR	<i>K_s</i>	20.92 ± 0.13	candidate 5	(17)
8.748	1200	...	GROND	<i>J</i>	>20.06	candidate 3	(17)
8.748	1200	...	GROND	<i>H</i>	20.51 ± 0.34	candidate 3	(17)
8.748	1200	...	GROND	<i>K_s</i>	>18.53	candidate 3	(17)
10.893	10×150	(80.020, 25.530)	LDT/LMI	<i>r'</i>	>24.9	candidate 3	(15)
10.893	10×150	(80.020, 25.530)	LDT/LMI	<i>i'</i>	24.8 ± 0.2	candidate 3	(15)
10.893	10×150	(80.025, 25.522)	LDT/LMI	<i>r'</i>	>25.1	candidate 4	(15)
10.893	10×150	(80.025, 25.522)	LDT/LMI	<i>i'</i>	>24.5	candidate 4	(15)
10.893	10×150	(79.999, 25.546)	LDT/LMI	<i>r'</i>	>25.1	candidate 5	(15)
10.893	10×150	(79.999, 25.546)	LDT/LMI	<i>i'</i>	24.7 ± 0.2	candidate 5	(15)
15.627	16×200	...	NOT	<i>z</i>	>22.2	...	(17)
25.741	1800	...	REM	<i>r</i>	>19.8	...	(16)
25.741	1800	...	REM	<i>H</i>	>19.49	...	(16)

3. LONG TERM FOLLOW-UP AND AFTERGLOW CANDIDATES

All follow-up observations did not confirm any candidate as the afterglow counterpart associated with GRB 240219A.

4. NATURE OF THE BURST

Due to the unknown distance of this event, authors plot this GRB along the curve with various redshifts on the $E_{p,z}-E_{iso}$ diagram.

Based on Figure 5, authors deduce that for GRB 240219A to appear as an intrinsic Type-II GRB, its redshift is likely no less than approximately 1.5.

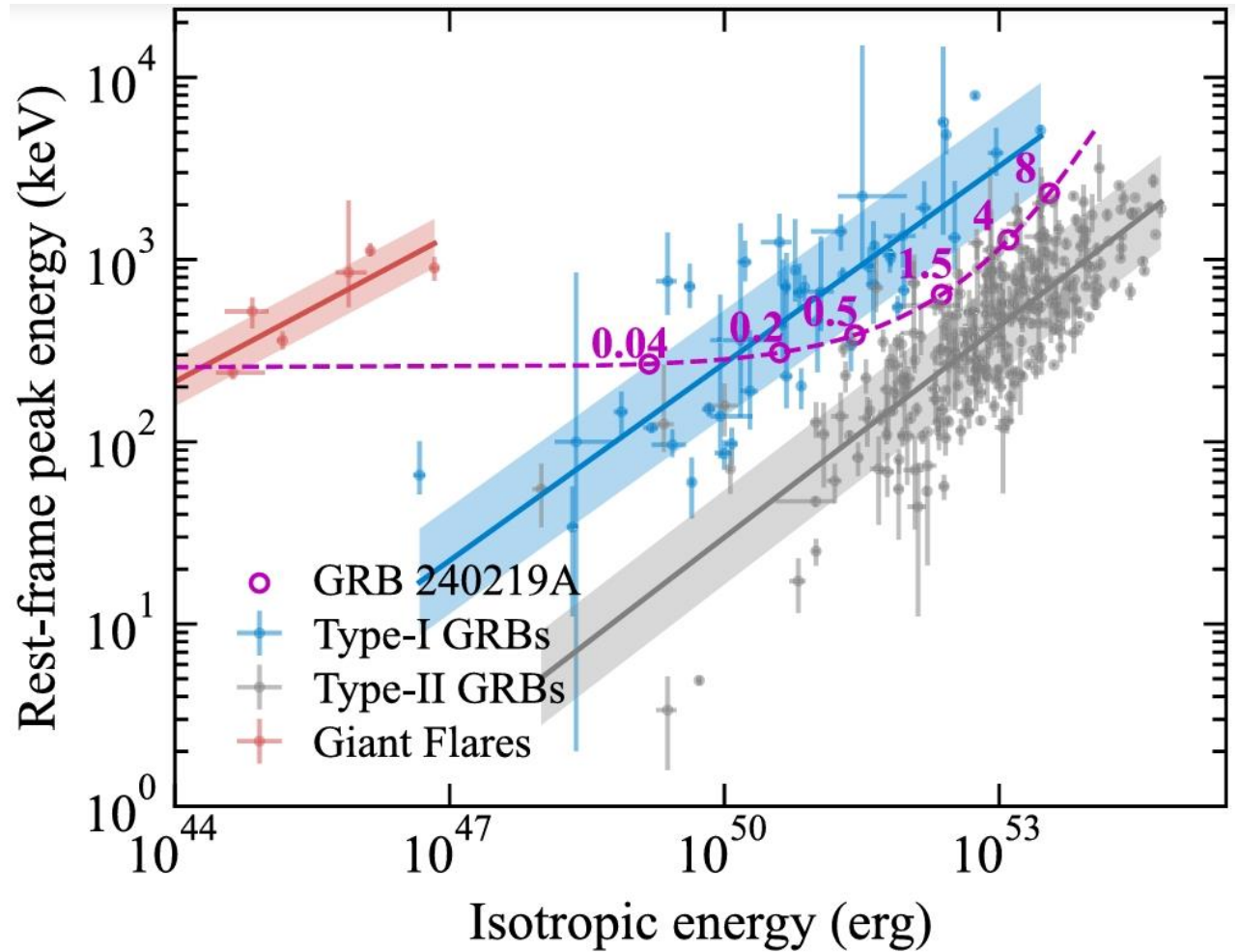


Figure 5. The $E_{p,z}-E_{iso}$ diagram. The blue, gray, and red solid lines represent the best-fit correlations for Type-I, Type-II, and magnetar giant flare populations, respectively. The purple dashed line indicates the position of GRB 240219A at various redshifts, with specific redshifts marked by dots. Error bars on data points represent the 1σ confidence level.

4.1 Classical Gamma-ray Burst, XRR, or X-ray flash?

In addition to the classical long/short dichotomy, GRBs have two special subclasses: X-ray flashes (XRFs) and X-ray riches (XRRs).

XRFs are characterized by stronger X-ray emission compared to classical gamma-ray bursts (C-GRBs).

XRRs occupy an intermediate position between XRFs and C-GRBs, displaying relatively softer gamma-ray emission than C-GRBs.

Classification of C-GRBs, XRRs, and XRFs:

- The spectral **peak energy**, E_p , is used as a criterion to distinguish between these subclasses. Sakamoto et al. established the boundary E_p at 30 keV between XRFs and XRRs, and at 100 keV between XRRs and C-GRBs.
- Alternatively, classify according to the **fluence ratio** in different bands, such as $S(25-50 \text{ keV})/S(50-100 \text{ keV})$ and $S(2-30 \text{ keV})/S(30-400 \text{ keV})$.

4.1 Classical Gamma-ray Burst, XRR, or X-ray flash?

The observed peak energy of the burst aligns with the typical values of Fermi/GBM detected GRB samples, categorizing it as a C-GRB.

However, the fluence ratio, $S(25\text{--}50\text{ keV})/S(50\text{--}100\text{ keV})$, is $0.85^{+0.15}_{-0.10}$, indicating that the burst is classified as an XRR, as illustrated in Figure 6.

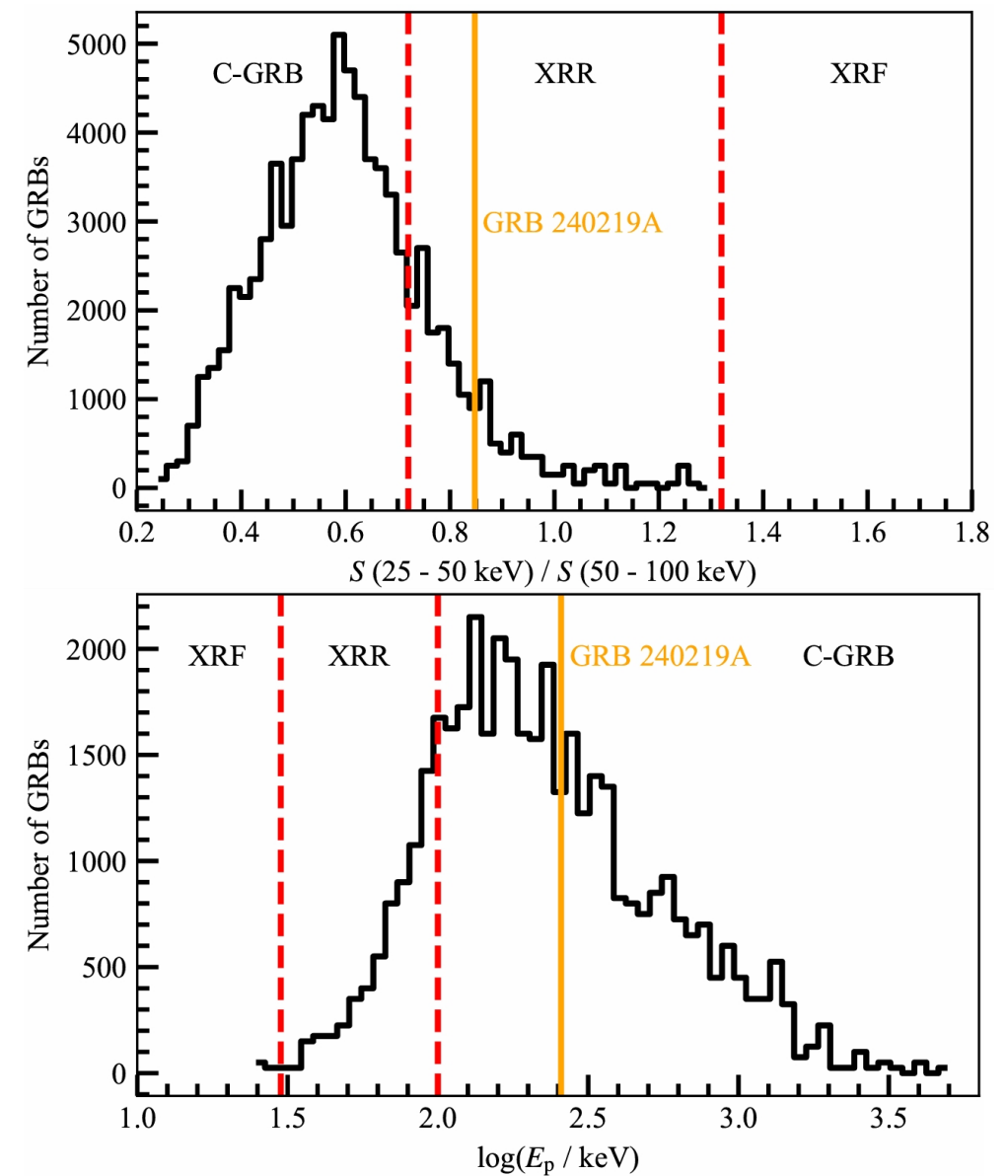


Figure 6. Fluence ratio and E_p distribution of Fermi/GBM-detected GRB samples. The red dashed vertical lines denote boundaries of GRB subclasses, labeled accordingly. Yellow vertical lines indicate the location of GRB 240219A on the plot.

4.1 C-GRB, XRR or XRF?

They further investigated the boundaries of the fluence ratio $S(25 - 50 \text{ keV})/S(50-100 \text{ keV})$ within the parameter space of the CPL model (see Figure 7).

There is a strong correlation between the fluence ratio and the observed spectral peak energy, particularly when the photon index α exceeds ~ -1.2 .

However, GRB 240219A exhibits a lower value of α , placing it in a controversial region where the fluence ratio fails to constrain a reasonable peak energy.

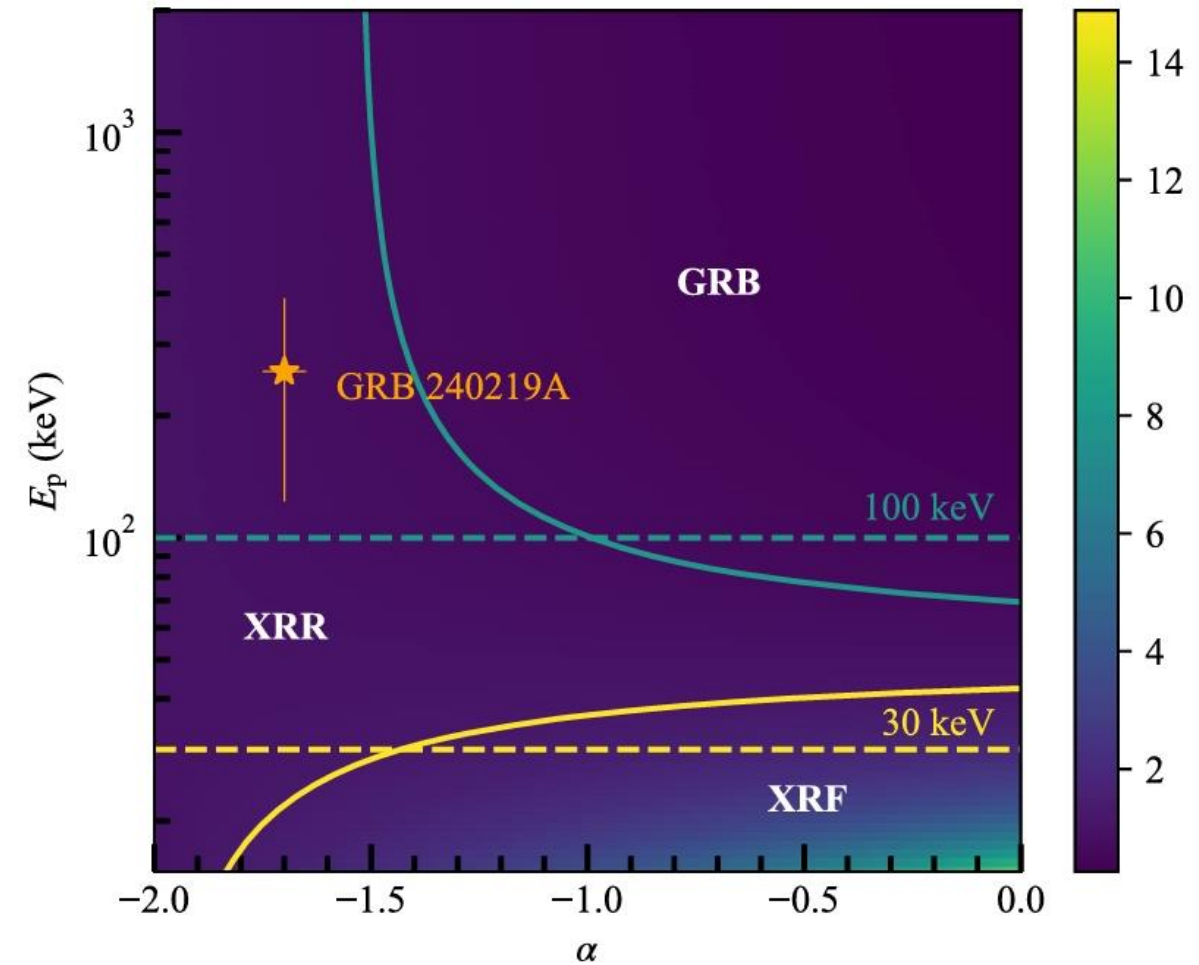


Figure 7. Fluence ratio distribution in the parameter space of the CPL model. The x - and y -axes represent the photon index and peak energy from the CPL model, respectively, with a color gradient indicating the corresponding fluence ratio. Solid curves delineate boundaries for fluence ratio subclassification criteria ($S(25-50 \text{ keV})/S(50-100 \text{ keV})$), while dashed horizontal lines indicate peak energy criteria. The location of GRB 240219A is marked with an orange star, with the error bar representing 1σ confidence level.

4.2. Implication of spectral components

The dimensionless entropy η and magnetization parameter $\sigma \equiv L_p/L_b$, where L_p is the Poynting luminosity and L_b is the baryonic luminosity, are two critical parameters governing the central engine dynamics.

When $\eta \gg 1$ and $\sigma \ll 1$, a dominant thermal photospheric emission component is expected.

Therefore, set $\eta=10^5$ and $\sigma=10^{-5}$ to generate the pure hot fireball component spectra. Figure 8 shows that significant thermal-like peaks deviate from the observed spectrum.

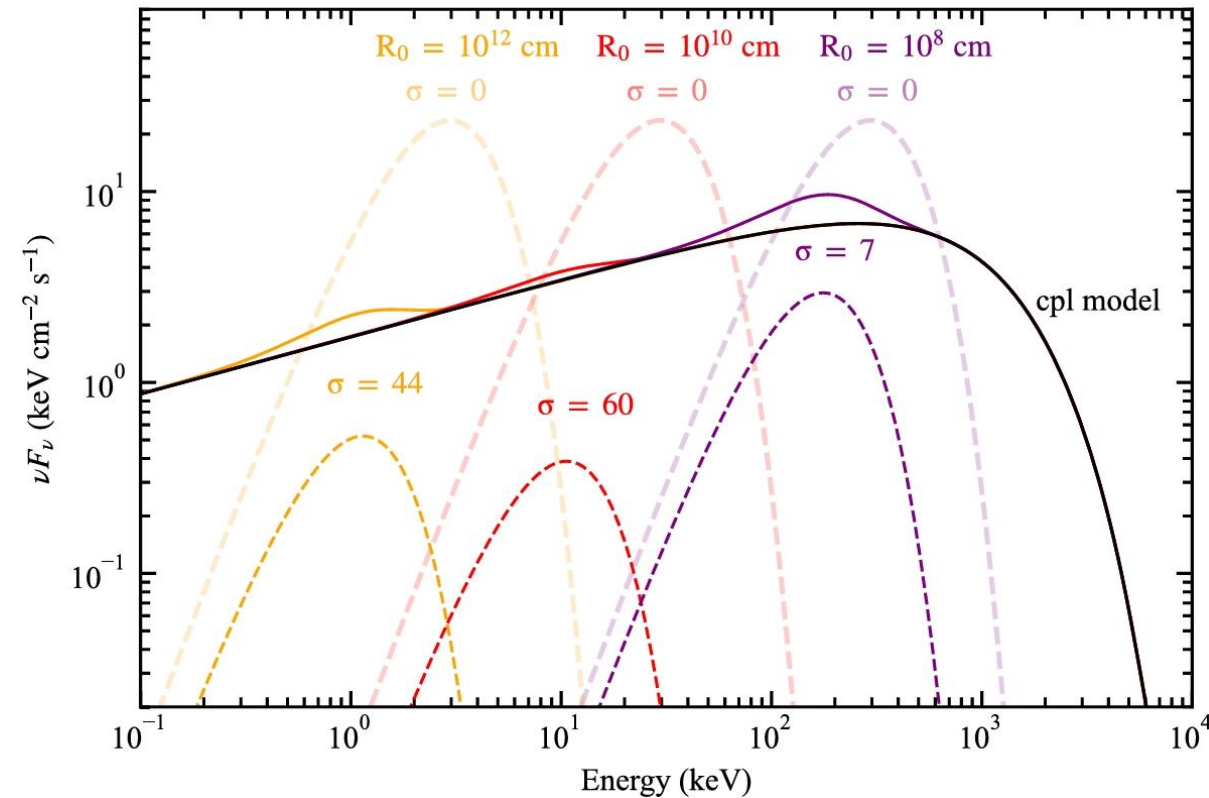


Figure 8. Calculation of the Poynting luminosity and baryonic luminosity ratio σ .

4.2. Implication of spectral components

The analysis suggests a significant magnetization of the central engine of GRB 240219A, with the majority of energy being carried by magnetic fields instead of photons in the hot outflow.

In this hybrid model, the parameters T_{obs} and F_{BB} are expressed as functions of η and σ .

In the study of hybrid jet components from a Fermi/GBM sample, the dimensionless entropy η for all bursts exhibits an average value of $\sim 10^3$. Therefore, they adopt $\eta=10^3$ in the hybrid model to constrain the value of σ .

The calculations reveal a lower limit of $\sigma \geq 7$ for $R_0 = 10^8$ cm, indicating that the outflow is mostly dominated by Poynting flux.

5. Conclusions

In this paper, authors report on the first EP detection of a bright X-ray flare, EP240219a, which is associated with an untriggered GRB with consistent trigger time and overall profile.

- The peak of the burst shows a delay between the detections by EP/WXT and Fermi/GBM.
- The spectral analysis shows that a single cutoff power-law model effectively describes the joint EP/WXT-Fermi/GBM spectra in general, indicating coherent broad emission typical of GRBs.
- Long-term observations identified several candidates in optical and radio wavelengths, none of which was confirmed as the afterglow counterpart during subsequent optical and near-infrared follow-ups.
- The analysis of GRB 240219A classifies it as an X-ray rich GRB with a high peak energy, presenting both challenges and opportunities for studying the physical origins of X-ray flashes (XRFs), X-ray rich GRBs (XRRs), and classical GRBs (C-GRBs).
- Linking the cutoff power-law component to nonthermal synchrotron radiation suggests that the burst is driven by a Poynting flux-dominated outflow.

Thanks